S. Haussener
Department of Mechanical and Process
Engineering,
ETH Zurich,
8092 Zurich, Switzerland

W. Lipiński
Department of Mechanical Engineering,
University of Minnesota,
Minneapolis, MN 55455

J. Petrasch
Department of Mechanical and Process
Engineering,
ETH Zurich,
8092 Zurich, Switzerland

P. Wyss
Department of Electronics/Metrology,
EMPA Material Science and Technology,
Überlandstrasse 129,
8600 Dübendorf, Switzerland

A. Steinfeld[1]
Department of Mechanical and Process
Engineering,
ETH Zurich,
8092 Zurich, Switzerland;
Solar Technology Laboratory,
Paul Scherrer Institute,
5232 Villigen, Switzerland
e-mail: aldo.steinfeld@eth.ch

Tomographic Characterization of a Semitransparent-Particle Packed Bed and Determination of its Thermal Radiative Properties

A two-phase medium consisting of densely packed large nonspherical semitransparent particles in a transparent fluid is considered. Its 3D digital geometry is obtained by computer tomography and employed to numerically calculate its porosity, specific surface, pore and particle size distributions, and the representative elementary volume for continuum domain. The collision-based Monte Carlo method is applied to calculate the probability distribution functions for attenuation path length and direction of incidence at the fluid-solid interface for each phase, which, in turn, are used to derive the extinction and scattering coefficients and the scattering phase functions. The methodology is applied to a packed bed of $CaCO_3$ particles, used in industrially relevant high-temperature processes. Spectral and directional dependencies of the radiative properties are analyzed. [DOI: 10.1115/1.3109261]

Keywords: packed bed, radiation, semitransparent, solar energy, chemical reactors

1 Introduction

Packed-bed reactors are commonly used in chemical processing because of their relatively high contacting area. Of special interest are packed beds for solar-driven thermochemical processes, e.g., the thermal and carbothermic reductions of ZnO [1,2] and the gasification of coal [3,4], which proceed above 1500 K using concentrated solar radiation as the energy source of high-temperature process heat. At these temperatures, thermal radiative transport becomes the dominant heat transfer mode. Thus, knowledge of the radiative properties of packed beds is crucial for the engineering design and optimization of these chemical reactors and processes. Experimental investigations of transmittance and extinction coefficients of porous media have been performed for foams and packed beds of opaque, transparent, and semitransparent phases [5–8]. Numerical simulation were carried out for artificially generated [9–16] and real [17,18] porous media by applying the radiative distribution function identification (RDFI) [9,17,18], Monte Carlo (MC) [15,16], two-flux [10–12], and discrete ordinate [13] methods.

In this paper, the RDFI method, calculated by MC, is applied to determine the radiative properties of a packed bed containing large nonspherical semitransparent particles. $CaCO_3$ particles (source: Carrara marble; Ferret's diameter=3 mm) have been selected for modeling because of their relevance in the high-temperature processing of lime, cement, and other material commodities, and in the capture of CO_2 from combustion flue gases [19].

Radiative characteristics of packed beds containing complex morphological structures may significantly deviate from those obtained when applying simplifying approximations, e.g., spherical particles. In this paper, computer tomography (CT) is applied to obtain the exact 3D geometrical representation of complex porous media composed of semitransparent phases. CT allows for nondestructive scanning of the structure in a single experimental run. In contrast to previous investigations [9–16], the CT-based methodology enables the determination of accurate effective radiative properties in the limit of geometric optics with negligible diffraction, which, in turn, can serve as reference values to those obtained by approximate methods.

2 Governing Equations

Radiative transfer in a quasicontinuous two-phase medium containing semitransparent phases can be described by two coupled equations of radiative transfer equations (RTEs) for phases i and j[2][18].

$$f_{v,i}\left[\frac{dI_i(s,\hat{\mathbf{s}})}{ds} + \beta_i I_i(s,\hat{\mathbf{s}})\right]$$

$$= f_{v,i}\left[n_i^2 \kappa_i I_{ib}(s,\hat{\mathbf{s}}) + \frac{\sigma_{s,ii}}{4\pi}\int_{4\pi} I_i(s,\hat{\mathbf{s}}_{in})\Phi_{ii}(\hat{\mathbf{s}},\hat{\mathbf{s}}_{in})d\Omega_{in}\right]$$

$$+ f_{v,j}\frac{\sigma_{s,ji}}{4\pi}\int_{4\pi} I_j(s,\hat{\mathbf{s}}_{in})\Phi_{ji}(\hat{\mathbf{s}},\hat{\mathbf{s}}_{in})d\Omega_{in}, \quad i,j=1,2; \ i\neq j$$

(1)

---

[1]Corresponding author.

[2]The spectral subscript λ is omitted for brevity.

where $\sigma_{s,i}$ and Φ_i are the internal scattering coefficient and internal scattering phase function of the bulk material forming phase i, $\sigma_{s,ii}$ and Φ_{ii} are those associated with internal reflections and internal scattering within phase i, and $\sigma_{s,ij}$ and Φ_{ij}, $i \neq j$, are those associated with radiation leaving phase i and entering phase j. Thus,

$$\sigma_{s,ii} = \sigma_{s,\text{refl},i} + \sigma_{s,i} \qquad (2)$$

$$\Phi_{ii} = \sigma_{s,ii}^{-1}(\Phi_{\text{refl},i}\sigma_{s,\text{refl},i} + \Phi_i\sigma_{s,i}) \qquad (3)$$

$$\beta_i = \kappa_i + \sigma_{s,ii} + \sigma_{s,ij} \qquad (4)$$

where $\sigma_{s,i}$, k_i, and Φ_i are determined by applying an appropriate theory, e.g., Mie. The two-phase medium morphology-associated properties $\sigma_{s,\text{refl},i}$, $\sigma_{s,ij}$, $\Phi_{\text{refl},i}$, and Φ_{ij} are determined by applying the MC methodology outlined below.

3 Methodology

The collision-based Monte Carlo ray-tracing method is used [20]. Characteristic size parameters $\xi = \pi d_h / \lambda \gg 1$ for both phases are assumed; thus, geometric optics is valid [21]. A large number of stochastic rays are launched within a representative elementary volume (REV). The rays are emitted isotropically and are uniformly distributed over REV. They undergo scattering/absorption internally and reflection/refraction at the fluid-solid interface. The distance between emission and collision points, and the direction of incidence at the interface are recorded for each ray. The following probability density and cumulative distribution functions, and the corresponding medium properties are then computed.

For the attenuation (extinction) path length within phase i,

$$F_{e,i} = \frac{1}{N_{\text{ray},i}} \sum_{k=1}^{N_{\text{ray},i}} \delta(s - s_k), \quad i = 1,2 \qquad (5)$$

$$G_{e,i}(s) = \int_0^s F_{e,i}(s^*)ds^* \approx 1 - \exp(-\beta_i s), \quad i = 1,2 \qquad (6)$$

For the absorption path length within phase i,

$$F_{a,i} = \frac{1}{N_{\text{ray},i}} \sum_{k=1}^{N_{\text{ray},i}} \delta(s - s_{a,k}), \quad i = 1,2 \qquad (7)$$

$$G_{a,i}(s) = \int_0^s F_{a,i}(s^*)ds^* \approx \frac{\kappa_i}{\beta_i}[1 - \exp(-\beta_i s)], \quad i = 1,2 \qquad (8)$$

For the scattering path length associated with refraction from phases i to j, and reflection and internal scattering within phase i,

$$F_{s,ij}(s) = \frac{1}{N_{\text{ray},i}} \sum_{k=1}^{N_{\text{ray},i}} \delta(s - s_{s,k}), \quad i,j = 1,2 \qquad (9)$$

$$G_{s,ij}(s) = \int_0^s F_{s,ij}(s^*)ds^* \approx \frac{\sigma_{ij}}{\beta_i}[1 - \exp(-\beta_i s)], \quad i,j = 1,2 \qquad (10)$$

For the direction of incidence at the phase interface within phase i,

$$F_{\mu_{\text{in}},i} = \frac{1}{N_{\text{att},i}} \sum_{k=1}^{N_{\text{att},i}} \delta(\mu_{\text{in},i} - \mu_{\text{in},i,k}), \quad i = 1,2 \qquad (11)$$

$$\Phi_{ij}(\mu_s) = \frac{2\int_{\mu_{\text{in}}=0}^1 \int_{\varphi_d=0}^\pi \int_{\mu_{\text{refl}}=0}^1 \delta(\mu_s - \sqrt{(1-\mu_{\text{in}}^2)(1-\mu_{\text{refl}}^2)} \cdot \cos \varphi_d - \mu_{\text{in}}\mu_{\text{refl}}) \cdot \rho''(\mu_{\text{in}},\mu_{\text{refl}},\varphi_d)F_{\mu_{\text{in}},i}\mu_{\text{refl}}d\mu_{\text{refl}}d\varphi_d d\mu_{\text{in}}}{\int_{\mu_{\text{in}}=0}^1 \int_{\varphi_d=0}^\pi \int_{\mu_{\text{refl}}=0}^1 \rho''(\mu_{\text{in}},\mu_{\text{refl}},\varphi_d)F_{\mu_{\text{in}},i}\mu_{\text{refl}}d\mu_{\text{refl}}d\varphi_d d\mu_{\text{in}}}, \quad i = j = 1,2 \qquad (12)$$

$$\Phi_{ij}(\mu_s) = \frac{2\int_{\mu_{\text{in}}=0}^1 \int_{\varphi_d=0}^\pi \int_{\mu_t=0}^1 \delta(\mu_s - \sqrt{(1-\mu_{\text{in}}^2)(1-\mu_t^2)} \cdot \cos \varphi_d - \mu_{\text{in}}\mu_t) \cdot (1 - \rho''(\mu_{\text{in}},\mu_t,\varphi_d))F_{\mu_{\text{in}},i}\mu_t d\mu_t d\varphi_d d\mu_{\text{in}}}{\int_{\mu_{\text{in}}=0}^1 \int_{\varphi_d=0}^\pi \int_{\mu_t=0}^1 (1 - \rho''(\mu_{\text{in}},\mu_t,\varphi_d))F_{\mu_{\text{in}},i}\mu_t d\mu_t d\varphi_d d\mu_{\text{in}}}, \quad i \neq j = 1,2 \qquad (13)$$

In Eqs. (5)–(13), $N_{\text{ray},i}$ is the number of rays launched in phase i within REV, and $N_{\text{att},i}$ is the number of rays attenuated in phase i at the phase interface.

4 Application to a Packed Bed of CaCO₃ Particles

4.1 Morphology Characterization. *Computer tomography.* The sample consists of a packed bed of nonspherical $CaCO_3$ particles randomly placed in a 4.5 cm-diameter rubber tube, as seen in Fig. 1(a). The sample is exposed to a polychromatic X-ray beam, generated by electrons incident on a wolfram target and filtered by a 0.0025 mm Re filter. The generator is operated at an acceleration voltage of 140 keV and a current of 0.11 mA. A

Hamamatsu flatpanel C7942 CA-02 protected by a 0.1 mm brass filter is used to detect the transmitted X-rays. The sample is scanned at 600 angles (projections). Each projection is an average over 8 scans with exposure time of 0.25 s, leading to a voxel size of 45 μm. Figures 1(b) and 1(c) show the 2D tomographic image and the 3D surface rendering of the sample, respectively.

The histogram of the normalized absorption values $\alpha/\alpha_{\max}$, shown in Fig. 2, reveals two distinct peaks that account for the solid and fluid (void) phases. The calculated and nearly identical width of the two peaks supports the assumption of homogeneity. The calculated minimum between the two peaks ($\alpha/\alpha_{\max}=0.43$) is used as threshold value for phase identification. Phase boundaries between two $CaCO_3$ particles are neglected, as they cannot be distinguished in the tomography images.
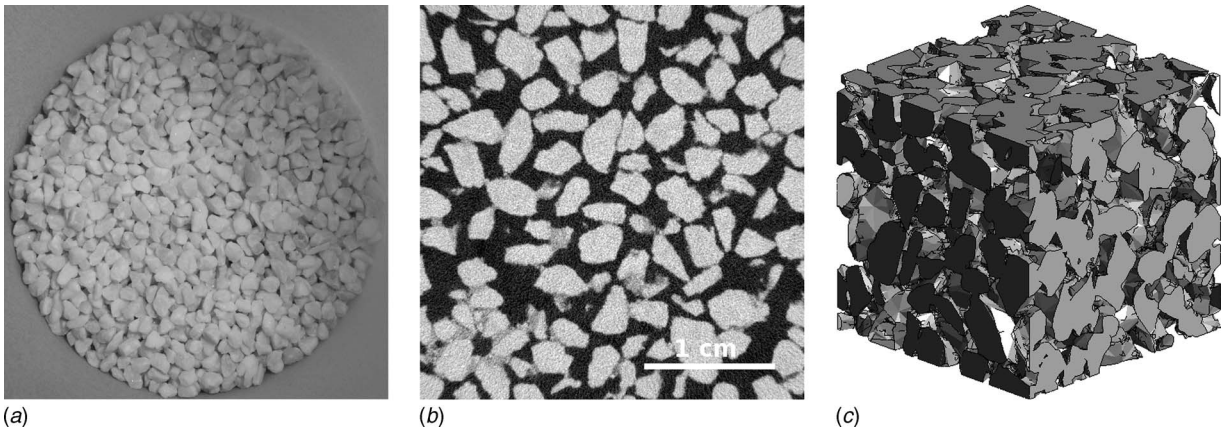
Fig. 1 Sample of the packed bed of CaCO₃ particles: (*a*) top view photograph, (*b*) 2D tomographic image, and (*c*) 3D surface rendering
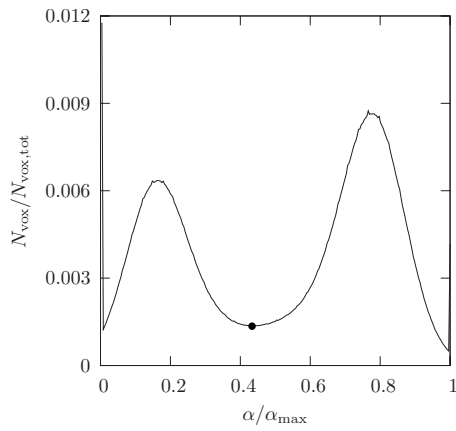

Fig. 2 Normalized histogram of the sample's absorption values obtained by CT for the void phase (left peak) and for the solid phase (right peak). The bullet indicates the threshold value $\alpha/\alpha_{max}=0.43$ used for phase identification.

Porosity and specific surface. The two-point correlation function indicates the probability of two points separated by a distance r to be in the void phase, given by [22,23]

$$s_2(r) = \frac{\int_V \int_{4\pi} \psi(\mathbf{r})\psi(\mathbf{r}+r\hat{\mathbf{s}})d\hat{\mathbf{s}}d\mathbf{r}}{4\pi V} \quad (14)$$

where ψ is the pore-space indicator function (=1 if the point lies within the void space; =0 if it lies within the solid phase). The specific surface area and porosity are calculated from [22]

$$\left.\frac{ds}{dr}\right|_{r=0} = -\frac{A_0}{4} \quad (15)$$

$$\lim_{r\to\infty} s_2(r) = \varepsilon^2 \quad (16)$$

$$s_2(0) = \varepsilon \quad (17)$$

Figure 3(*a*) shows the two-point correlation function for the CaCO₃ packed bed. The calculated porosity is 0.39, which compares well with the porosity determined experimentally from the sample weight 0.40 ± 0.02. This value is close to the one for a
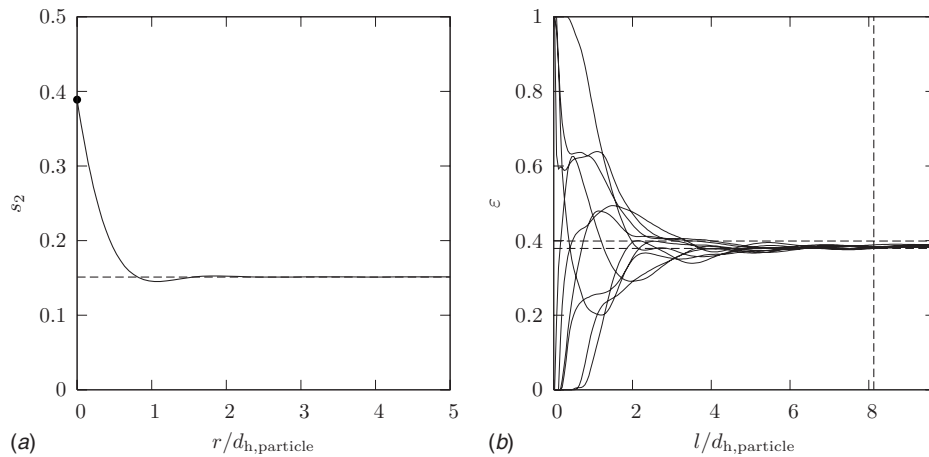

Fig. 3 (*a*) Two-point correlation function for the CaCO₃ packed bed. The value at $r=0$ corresponds to the bed porosity. The dashed line indicates the asymptotic value of the function, which corresponds to ε^2. (*b*) Determination of the REV edge length (indicated by the vertical dashed line) by calculating the porosity of ten subvolumes with varying edge lengths *l* at random locations. The tolerance band for conversion and determination of the REV volume at $\varepsilon\pm0.01$ is indicated by the two horizontal dashed lines.
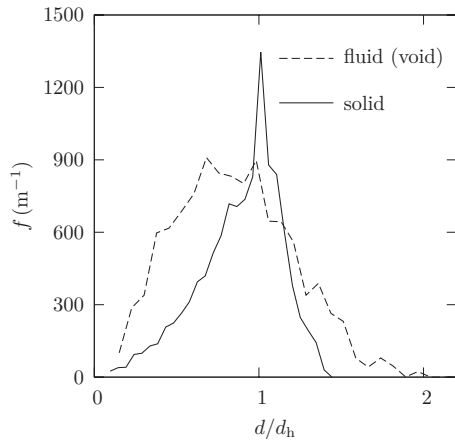
Fig. 4 Opening size distribution functions, $f=-d\varepsilon_{op}(d)/(\varepsilon_\infty dd)$ of the solid and fluid phases of the CaCO$_3$ packed bed ($d_h \equiv d_{h,pore}$ for fluid and $d_h \equiv d_{h,particle}$ for solid)

dense random or orthorhombic packed bed made of uniform monodispersed spheres [24]. The calculated specific surface area is 1.31×10^3 m^{-1}, which corresponds to an analytically calculated particle diameter of 2.8 mm for uniform monodispersed spheres. As will be shown later, the hydraulic particle diameter for the randomly shaped CaCO$_3$ particles lies around 1.9 mm.

Table 1 Arithmetic mean diameter, mode, median, and hydraulic diameter calculated from the pore and particle size distributions

	Pore	Solid
Arithmetic mean (mm)	1.00	1.66
Mode (mm)	0.81	1.89
Median (mm)	0.98	1.75
Hydraulic diameter (mm)	1.19	1.87

Representative elementary volume. REV indicates the minimum volume for which the continuum assumption is still valid. REV is determined based on the porosity for subvolume sizes at ten random locations in the sample, as indicated in Fig. 3(*b*). Note that for an edge length *l* approaching zero, the porosity is either 0 or 1, depending whether the point lies in the void or the solid phase. Assuming a tolerance band of ± 0.01, $l_{REV}=0.0152$ m (for ± 0.02, $l_{REV}=0.0105$ m; for ± 0.05 $l_{REV}=0.0054$ m) and is used as the minimum sample size in the following analysis.

Pore and particle size distributions. Opening, a mathematical morphology operation consisting of erosion followed by dilation using the same structuring element, is applied to calculate the pore and particle size distributions, i.e., the size distribution defined by the sphere that fits completely within the pore or particle space, respectively. Figure 4 shows the distribution functions of the pore and particle sizes. The median, mode, mean, and hydraulic diameters $d_{h,particle}=4\varepsilon/A_0$ and $d_{h,pore}=4(1-\varepsilon)/A_0$ are listed in Table 1. Thus, the assumption of geometrical optics is valid for $\lambda < 3500$ μm.

4.2 Radiative Properties. In this section, the void phase and the CaCO$_3$ particles of the packed bed are referred to as fluid and solid phases, respectively. The corresponding phase indices i,j used in Eqs. (5)–(13) are 1 for the fluid phase and 2 for the solid phase. Spectral calculations of the radiative properties are performed for 150 distinct points between 0.1 μm and 100 μm. Reflection and refraction at the specularly reflecting and diffusely reflecting interfaces are modeled by Fresnel's equations and diffuse reflection/refraction, respectively.

Single-phase internal radiative properties. The fluid phase is assumed to be transparent, i.e., its internal absorption and scattering coefficients $\sigma_{s,1}$ and κ_1, respectively, are equal to zero, and its refractive index is equal to 1. The bulk properties of CaCO$_3$ are determined based on the properties of CaCO$_3$ grains (monocrystals). They are randomly shaped and oriented, as seen in the scanning electron microscope (SEM) photograph of Fig. 5. Their characteristic size is 160 μm. Figure 6 shows the complex refractive index $m_2=n_2-ik_2$ of CaCO$_3$ [25]. In the spectral range 0.2–6 μm, the imaginary part was obtained by applying the Lorentz theory [26].
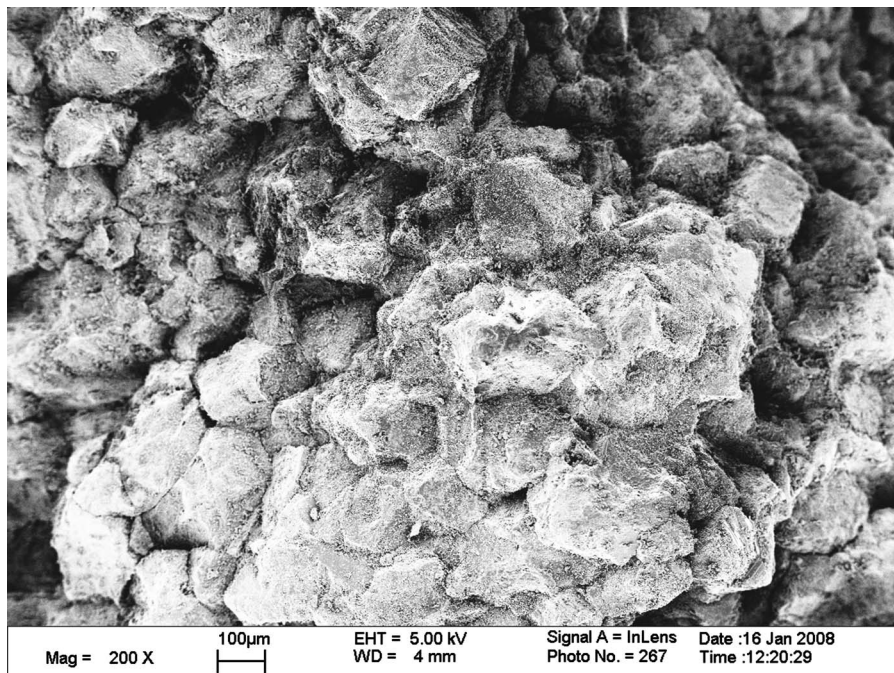

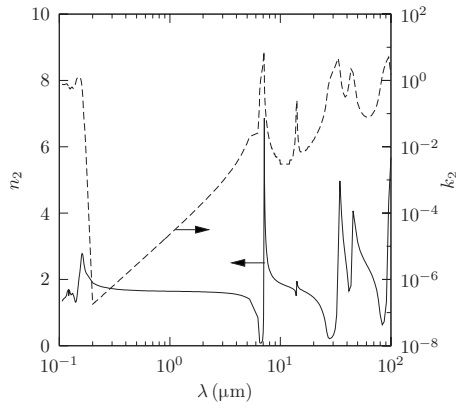**Fig. 5 SEM picture of a single CaCO$_3$ particle**

Fig. 6 Complex refractive index of CaCO$_3$: (solid line) real part obtained experimentally [25], and (dashed line) imaginary part obtained by the Lorentz theory in the spectral range 0.2–6 μm [26] and experimentally in the remaining range [25]

Fig. 8 Internal absorption and scattering coefficients of CaCO$_3$ particles

The directional-hemispherical reflectivities at the specular fluid-solid interface for radiation incident from the fluid phase $\rho_{sp,12}$ and for radiation incident from the solid phase $\rho_{sp,21}$ are calculated using Fresnel's equations [21]. The hemispherical reflectivities of both sides of a diffuse fluid-solid interface ρ_d are equal to that for a diffuse CaCO$_3$ surface [27]. For $\lambda < 0.8$ μm and $\lambda > 2.5$ μm, the hemispherical reflectivity is extrapolated with constant values 0.85 and 0.87, respectively. $\rho_{sp,12}$, $\rho_{sp,21}$, and ρ_d are shown in Fig. 7 as a function of wavelength.

The internal radiative coefficients of CaCO$_3$, $\sigma_{s,2}$, and κ_2, obtained by applying the Mie theory, are shown in Fig. 8 [28]. The spectral oscillations, particularly for $\lambda > 6$ μm, result from oscillations in the complex refractive index (see Fig. 6). The internal scattering within CaCO$_3$ is assumed isotropic ($\Phi_2 = 1$). Figure 9 shows the ratio of the scattering efficiency factor for dependent scattering, calculated by gas, packed-sphere, liquid, or modified-liquid model [29], to that for independent scattering calculated by Mie theory (assumed $f_v = 1$). Dependent scattering effects are thus neglected in this study since the maximal reduction in the scattering efficiency factor for 100 μm > λ > 0.1 μm is only about 10%.

Two-phase medium radiative coefficients. The scattering coefficients of the CaCO$_3$ packed-bed two-phase medium are shown in Fig. 10 as a function of wavelength for the fluid phase (Figs. 10(a)

and 10(b)) and the solid phase (Figs. 10(c) and 10(d)), assuming specularly reflecting particles (Figs. 10(a) and 10(c)) and diffusely reflecting particles (Figs. 10(b) and 10(d)). The reflection behavior of the fluid-solid interface significantly influences $\sigma_{s,ij}$ and $\sigma_{s,refl,i}$. For the fluid phase and specular interface, $\sigma_{s,refl,i} < \sigma_{s,ij}$ for $\lambda < 6$ μm, while for the diffuse interface $\sigma_{s,refl,i} > \sigma_{s,ij}$. For the solid phase, $\sigma_{s,refl,i} > \sigma_{s,ij}$, and this trend is independent of the reflection interface type. $\sigma_{s,refl,1}$, obtained for the specular and diffuse interfaces, clearly follows the shape of ρ_{sp} and ρ_d, respectively (see Fig. 7). $\sigma_{s,refl,2}$ and $\sigma_{s,21}$ are additionally influenced by the presence of the total reflection phenomenon in the particle. Obviously, for any phase, $\sigma_{s,ij}$ is complementary to $\sigma_{s,refl,i}$ since it refers to the transmitted portions of radiation across the interface.

The extinction coefficients β_i are shown in Fig. 11. They are independent of the interface reflection type (specular/diffuse). In addition, β_1 is independent of λ as it is a function of the interface geometry only. β_2 increases with λ because of the increasing $\kappa_2 + \sigma_{s,2}$. The spectral oscillations in β_1 result from the statistical MC oscillations. The spectral oscillations in β_2 are mostly the result of the spectral oscillations of κ_2 and $\sigma_{s,2}$ (see Fig. 8).

Two-phase medium scattering phase functions. The probability density functions of the directional cosine of the incidence angle at the fluid-solid interface, determined by MC, are plotted in Fig. 12 for both phases. Assuming $\kappa_2 = \sigma_{s,2} = 0$, $F_{\mu_{in},1}$ and $F_{\mu_{in},2}$ compare well to $F_{\mu_{in}}$, computed for identical overlapping opaque spheres (IOOS) and for identical overlapping transparent spheres
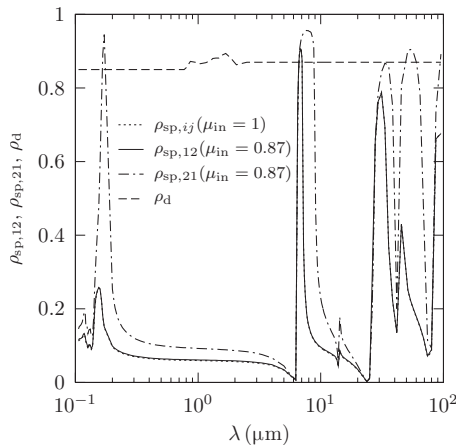

Fig. 7 Spectral directional-hemispherical reflectivities at the specular fluid-solid interface for selected incidence directions, and spectral hemispherical reflectivity of the diffuse fluid-solid interface
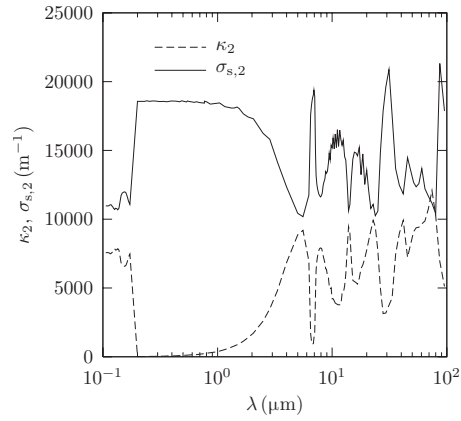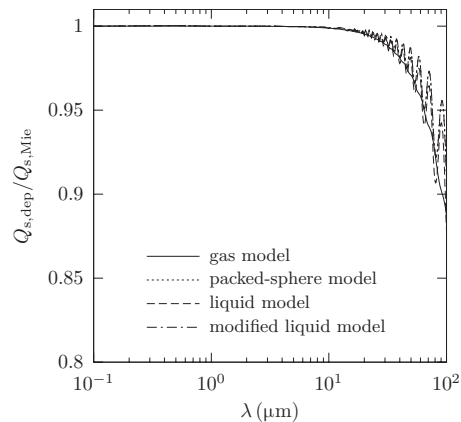

Fig. 9 Ratio of the scattering efficiency factor obtained for dependent scattering calculated by gas, packed-sphere, liquid, and modified-liquid models to that obtained for independently scattering calculated by the Mie theory
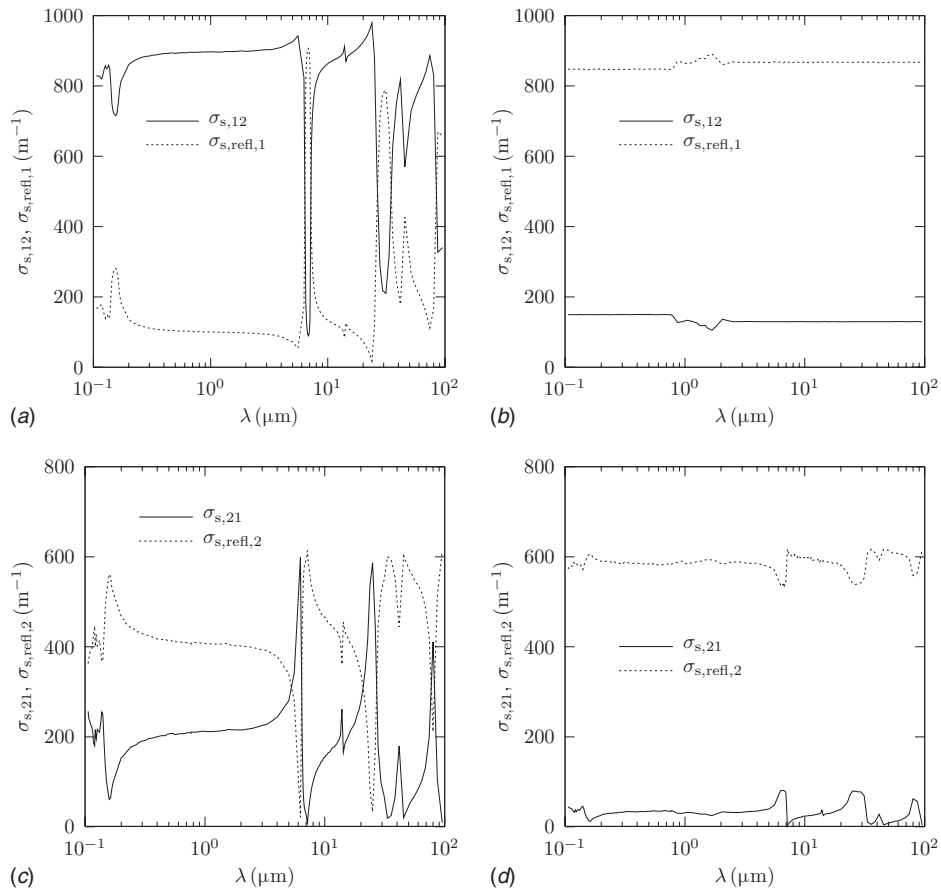
Fig. 10 Spectral scattering coefficients of the CaCO₃ packed bed for ((a) and (b)) the fluid phase and ((c) and (d)) the solid phase, assuming ((a) and (c)) specularly reflecting particles and ((b) and (d)) diffusely reflecting particles

(IOTS), respectively [9,17]. For the real values of κ_2 and $\sigma_{s,2}$, $F_{\mu_{in},2}$ depends weakly on β_2 and hence on λ. The dependency of $F_{\mu_{in},2}$ on β_2 is explained by the fact that, for increasing β_2, the incidence angles corresponding to longer paths occur less frequently. Functions $F_{\mu_{in},i}$ are then used to calculate the scattering phase functions by applying Eqs. (12) and (13).

Figures 13 and 14 show the scattering phase functions for spectral and diffuse interfaces, respectively, as a function of the cosine of the scattering angle at selected wavelengths $\lambda = 0.1$ μm, 1 μm,

10 μm, and 100 μm. Φ_{12} and Φ_{21} are identical for the specularly reflecting solid-fluid interface because the Fresnel's equation gives the same results when the angle of incidence and transmission are interchanged [21]. The forward scattering peak decreases with λ due to increasing normal-hemispherical reflectivity of the interface, which in turn is the result of the increasing n_2 and k_2. Since total reflection is assumed for the diffuse interface, $\Phi_{21} = 0$ for $\mu_s < -\sqrt{1 - \mu_{refl,tot}^2}$. For the specular interface, $\Phi_{refl,1}$ and $\Phi_{refl,2}$ are clearly functions of λ due to the spectral variation of ρ_{sp}, while
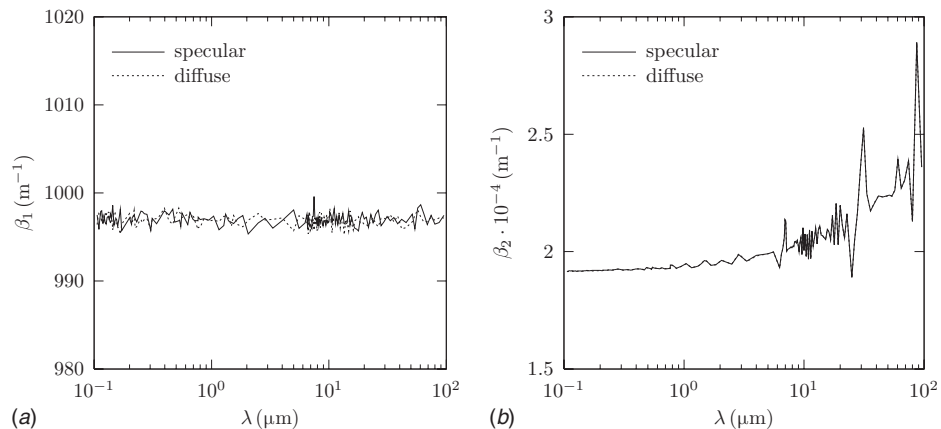

Fig. 11 Spectral extinction coefficients of the packed bed: (a) fluid phase and (b) solid phase
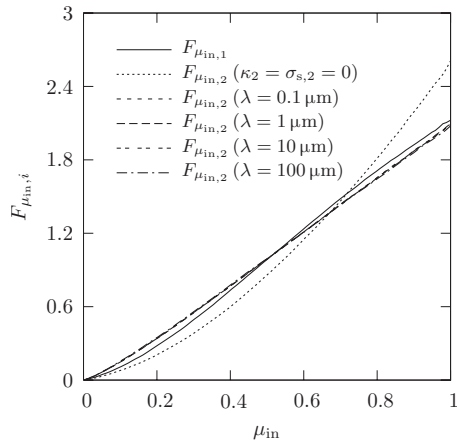
Fig. 12 Probability density functions of the directional cosine of the incident angle at the fluid-solid interface for selected wavelengths

this cannot be observed for the diffuse interface. The jump of $\Phi_{\mathrm{refl},2}$ is explained by enhanced interface reflections for $\mu_s > \sqrt{1 - \mu_{\mathrm{refl,tot}}^2} - \mu_{\mathrm{refl,tot}}$. Obviously, Φ_{11} is equal to $\Phi_{\mathrm{refl},1}$ because of the absence of internal scattering in the fluid

phase. In contrast, Φ_{22} is mostly influenced by Φ_2 because of the large internal scattering in the solid phase (see Eq. (3)).

Sensitivity analysis. A MC parametric study is carried out to elucidate the influence of the uncertainties in n_2, k_2, and ρ_d on the radiative properties by varying by $\pm 20\%$ their reference values $n_2 = 1.64$, $k_2 = 2.3 \times 10^{-5}$, and $\rho_d = 0.87$ at $\lambda = 1$ μm. These variations do not affect β_i ($<1\%$ change). κ_2 is influenced by variations of k_2 (up to 20%) and n_2 (6%) for specular and diffuse fluid-solid interfaces. For the specular interface, variation of n_2 leads to remarkable effect on $\sigma_{s,\mathrm{refl},1}$, $\sigma_{s,\mathrm{refl},2}$, $\sigma_{s,12}$, and $\sigma_{s,21}$ (up to 66% change), because ρ_{sp} depends on n_2. For diffusely reflecting particles, variation of n_2 and k_2 leads to only small variations in $\sigma_{s,\mathrm{refl},1}$, $\sigma_{s,\mathrm{refl},2}$, and $\sigma_{s,12}$ (up to 5% change) due to the varying particle optical thicknesses and the total reflection angles. The change in $\sigma_{s,21}$ is up to 55%. The variation of ρ_d has a more pronounced effect on the scattering coefficients. For example, for $\rho_d = 1.0$ (no refraction), $\sigma_{s,ij} = 0$, while reduction in ρ_d by 20% nearly doubles $\sigma_{s,ij}$. Decreasing values of n_2 augments the forward scattering peaks of Φ_{12} and Φ_{21} for both specular and diffuse interfaces, as seen in Fig. 15. This is due to smaller relative angles between the incident and refracted rays for both specular and diffuse interfaces, according to Fresnel's equations. Variations of k_2 and ρ_d by $\pm 20\%$ do not affect the scattering phase functions. Variation of n_2 has an effect on $\Phi_{\mathrm{refl},1}$ and $\Phi_{\mathrm{refl},2}$ for the specular interface because the shape of $\rho_{sp}(\mu_{\mathrm{in}})$ depends on n_2. Specular reflection generally leads to more pronounced forward scattering
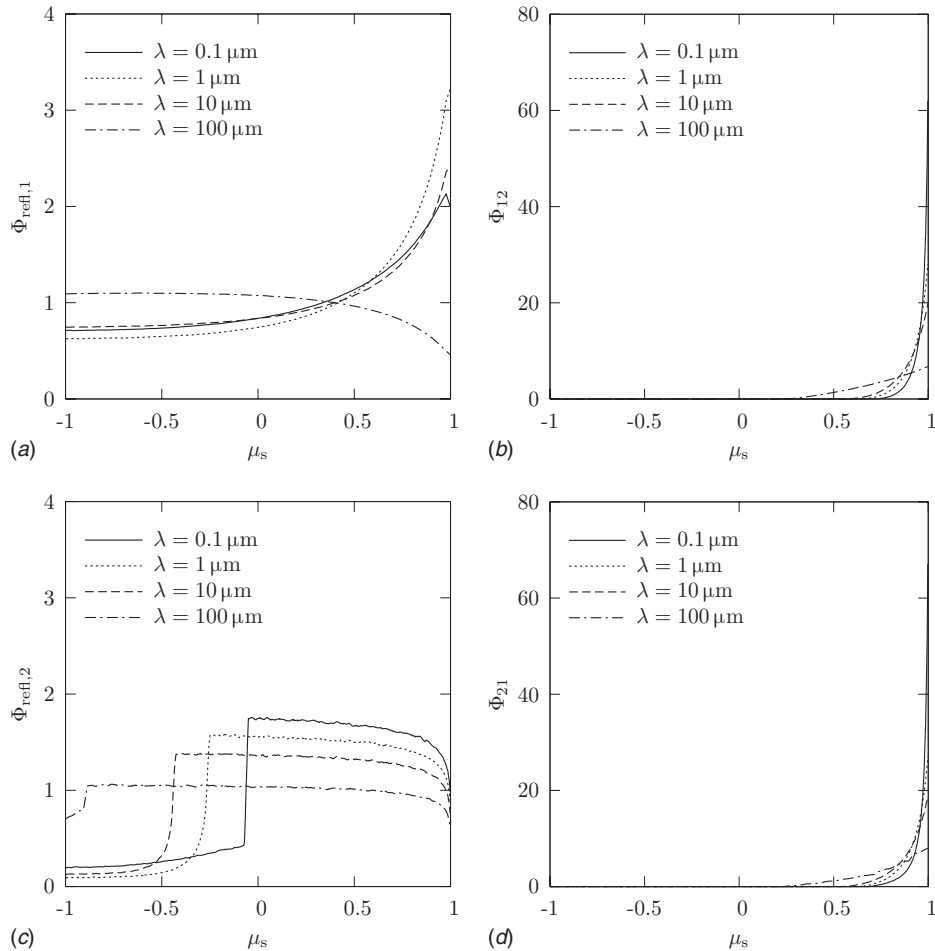

Fig. 13 Scattering phase functions of the CaCO₃ packed bed versus cosine of the scattering angle for a specularly reflecting solid-fluid interface, at selected wavelengths $\lambda = 0.1$ μm, 1 μm, 10 μm, and 100 μm
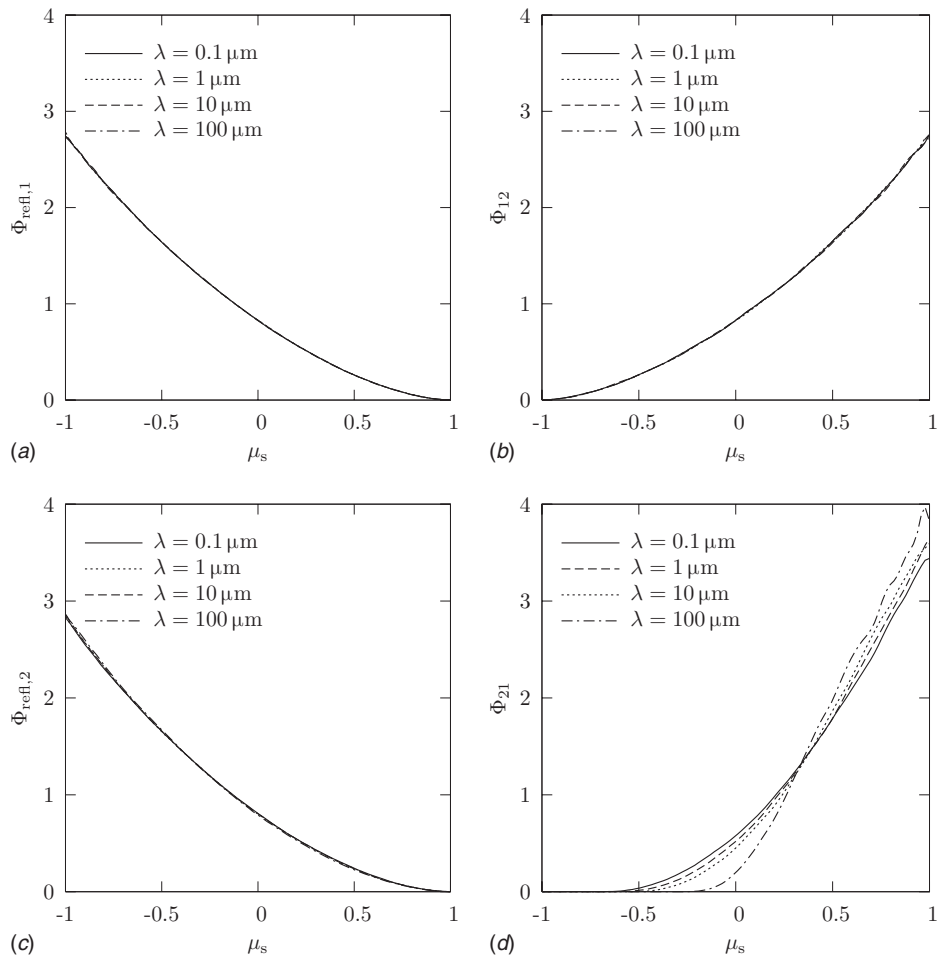
Fig. 14 Scattering phase functions of the CaCO₃ packed bed versus cosine of the scattering angle for a diffusely reflecting solid-fluid interface, at selected wavelengths λ=0.1 μm, 1 μm, 10 μm, and 100 μm

in $\Phi_{\mathrm{refl},1}$ and $\Phi_{\mathrm{refl},2}$, mainly as a result of the enhanced reflective behavior of the interface at larger incidence angles, while backward scattering is favored for diffusely reflecting particles. This behavior is less evident for materials with higher β_2 and $\sigma_{s,2}$, respectively, since the fraction of internal (isotropic) scattering is
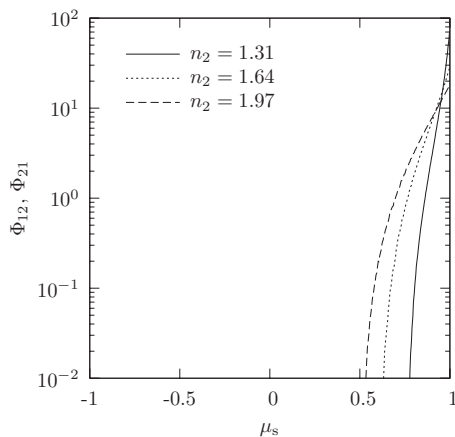

Fig. 15 Scattering phase function Φ_{12} and Φ_{21} for specular and diffuse fluid-solid interfaces, as a function of the scattering angle cosine, for selected refractive indices n_2=1.31, 1.64, and 1.97

larger. Sensitivity analysis of the statistically determined characteristic size of the grains indicates that reduced grain size enhances the variations in the extinction behavior for wavelengths above 10 μm, while the opposite is true for larger grain sizes. Changing the characteristic size by ±20% leads to variations in the extinction efficiency of up to 13%, scattering efficiency of up to 25%, and absorption efficiency of up to 19%.

Accuracy and validation of the MC algorithm. MC convergence is examined for 2-norms of $F_{\mu_{\mathrm{in}},i}$, $G_{e,i}$, $G_{a,i}$, and $G_{s,ij}$ for 10^4, 10^5, 10^6, 10^7, and 10^8 stochastic rays, normalized with respect to the reference solution for 10^9 rays, $\epsilon = \|\bar{y} - \bar{y}_{\mathrm{ref}}\|_2 / \|\bar{y}_{\mathrm{ref}}\|_2$, with $\bar{y}$ being the computed vector of the corresponding cumulative distribution function for the corresponding number of rays. The results are shown for the selected functions in Fig. 16. ϵ decrease exponentially with N_{ray}. The maximum $\epsilon=1.3$, obtained for $F_{\mu_{\mathrm{in}},2}$ using $N_{\mathrm{ray}}=10^4$, decreases to 1.2×10^{-2} using $N_{\mathrm{ray}}=10^8$. ϵ is relatively high for $F_{\mu_{\mathrm{in}},2}$ because of the large values of the optical thickness inside the particles, which leads to a small number of rays reaching particle boundaries and, consequently, high uncertainties in $F_{\mu_{\mathrm{in}},2}$.

The MC algorithm was used to calculate the radiative characteristics of an independently scattering particle cloud of large opaque spheres for $f_v=1.6 \times 10^{-3}$, $d=2$ μm, $n=1.64$, and $k=2.6 \times 10^{-5}$ at $\lambda=1$ μm. The scattering phase functions for diffusely reflecting and specularly reflecting particle surfaces are plotted in Fig. 17. Also shown are the corresponding phase functions obtained analytically [21].
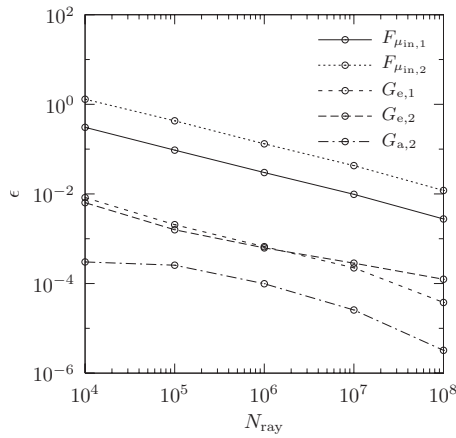
Fig. 16 Normalized two-norm of the cumulative distribution functions

Fig. 18 Normalized mean intensity along three orthogonal directions as a function of sample length

$$\Phi_{\text{refl},1,\text{d,an}}(\mu_s) = \frac{8}{3\pi}(\sqrt{1-\mu_s} - \mu_s \arccos(\mu_s)) \qquad (18)$$

$$\Phi_{\text{refl},1,\text{sp,an}}(\mu_s) = \frac{\rho_{\text{sp}}(1/2(\pi - \arccos(\mu_s)))}{2 \int_0^1 \rho_{\text{sp}}(\mu_{\text{in}})\mu_{\text{in}}d\mu_{\text{in}}} \qquad (19)$$

The scattering and extinction coefficients can be calculated analytically [21] as follows:

$$\sigma_{s,\text{an}} = \frac{3}{2}\frac{f_v}{d}Q_s \qquad (20)$$

$$\beta_{\text{an}} = \frac{3}{2}\frac{f_v}{d}Q_e \qquad (21)$$

where $Q_{s,d}=\rho_d$, $Q_{s,\text{sp}}=\rho_{\text{sp}}$, and $Q_e=1$ for large spheres without diffraction [21]. The MC-computed scattering coefficients for diffuse and specular particles, and the extinction coefficients are 1071 m^{-1}, 126 m^{-1}, and 1237 m^{-1}, respectively; the analytically calculated ones are 1032 m^{-1}, 121 m^{-1}, and 1200 m^{-1}, respectively. Furthermore, the code was validated for IOOS and IOTS [17].

The anisotropy of the sample was examined by subdividing the volume domain in eight subvolumes and calculating β_i along each
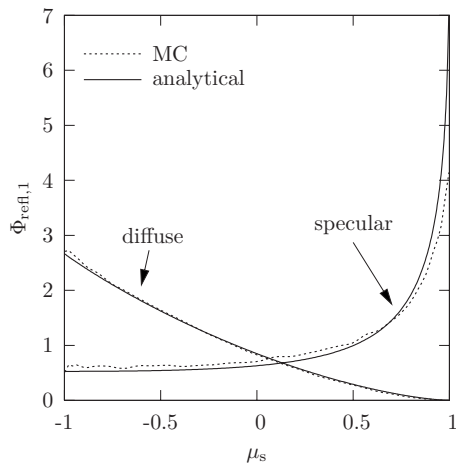

Fig. 17 MC (dashed line) and analytically (solid line) calculated phase functions of a particle cloud for $f_v = 1.6 \times 10^{-3}$, $d = 2$ μm, $n=1.64$, and $k=2.6 \times 10^{-5}$ at $\lambda = 1$ μm, $\rho_d = 0.866$, and for specularly and diffusively reflecting particles
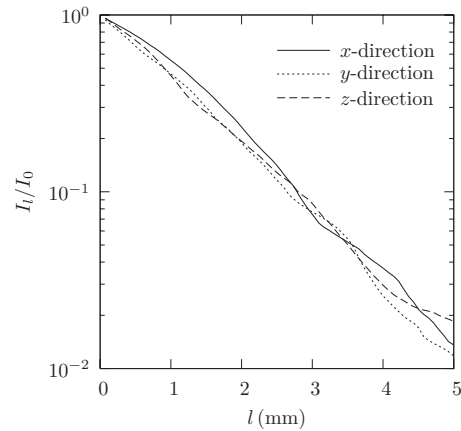
coordinate axis for each subvolume [17], assuming opaque particles. The results are presented in Fig. 18 and indicate the negligible role of the sample's anisotropy.

The MC algorithm was further used to compute the radiative characteristics of a cubic ($\varepsilon=0.48$) and orthorhombic ($\varepsilon=0.40$) packed bed of glass spheres ($n=1.5$, $k=0$ at $\lambda=0.6328$ μm) with diameter 1.269 mm. Since the glass particles are transparent at $\lambda=0.6328$ μm, $I_1(\hat{s})=I_2(\hat{s})$ [18] and $\beta_{\text{MC}}=\beta_1\varepsilon+\beta_2(1-\varepsilon)$. β_{MC} was calculated to be 1775 m^{-1} and 1952 m^{-1} for the cubic and orthorhombic bed configurations, respectively. The experimentally determined value for a randomly packed bed ($\varepsilon=0.42$) was $\beta_{\text{EX}} = 2326 \pm 416$ m^{-1} [6]. The strength of the CT-based methodology is that it can utilize the exact 3D geometry of porous media in the limit of the geometric optics with negligible diffraction. Once the accurate spectral bulk (microscale) radiative properties of the material and interface are known, the macroscale radiative properties can be determined with good accuracy.

5 Conclusions

A computational technique has been developed to study the thermal radiative properties of two-phase media containing densely packed large nonspherical semitransparent particles. The 3D digital geometry of a packed bed of CaCO$_3$ particles was obtained by employing CT and was used to directly determine medium morphological characteristics such as porosity, specific surface, pore and particle size distributions, and the REV for continuum domain. The collision-based MC method was applied to calculate the probability distribution functions of the attenuation path length and the direction of incidence at the fluid-solid interface for the fluid and solid phases, which, in turn, were used to obtain the radiative properties of the two-phase medium.

Spectral extinction coefficients were found to be independent on the reflectivity type (specular/diffuse) of the fluid-solid interface. In contrast, they depend strongly on the packed-bed geometry and the internal extinction coefficient $\sigma_{s,2}+\kappa_2$, which increases with wavelength due to the increasing complex refractive index. The scattering coefficients associated with refraction and reflection at the fluid-solid interface $\sigma_{s,ij}$ ($i \neq j$) and $\sigma_{s,\text{refl},i}$, respectively, depend on its morphology and reflective characteristics and on the internal radiative properties of the solid phase. $\sigma_{s,ij}$ and $\sigma_{s,\text{refl},i}$ behave complementary. Scattering functions related to the diffraction phenomenon Φ_{ij} ($i \neq j$) are restricted by total reflection. $\Phi_{\text{refl},i}$ strongly depends on wavelength for specularly reflecting interfaces, while the opposite is true for diffuse-reflecting interfaces. Forward scattering was found to be predominant for specular-reflecting particles, while backscattering is typical for

diffusely reflecting particles. Large internal extinction coefficient with isotropic internal scattering lead to less pronounced directional behavior of Φ_{ii}.

Directional determination of the extinction coefficient elucidated the negligible anisotropy of the sample. The MC algorithm was validated by computing the radiative properties of semitransparent porous media reported in the literature.

The methodology presented here can be generally applied for the determination of the radiative properties of porous materials of complex geometry, especially for low porosity media where measurements become difficult.

Acknowledgment

Nomenclature

A_0 = specific surface, m^{-1}
d = particle diameter, m
d_h = hydraulic diameter, m
f = size distribution function, m^{-1}
f_v = volumetric fraction
F = probability density function
G = cumulative distribution function
I = radiative intensity, $W\,m^{-3}\,sr^{-1}$
k = imaginary part of complex refractive index
l = length, m
m = complex refractive index
n = real part of complex refractive index
N_{ray} = number of rays
N_{att} = number of attenuated rays
N_{vox} = number of voxels
Q = efficiency factor
r = distance between two points in the sample, m
$\mathbf{r}$ = position vector for spatial coordinates in the sample, m
s = path length, m
$\hat{\mathbf{s}}$ = unit vector of path direction
s_2 = two-point correlation function
V = total sample volume, m^3

Greek

α = absorption values of tomographic scans, m^{-1}
β = extinction coefficient, m^{-1}
δ = Dirac delta function
ε = porosity
κ = absorption coefficient, m^{-1}
λ = radiation wavelength, m
μ_{in} = cosine of incidence angle
μ_{refl} = cosine of reflection angle
μ_s = cosine of scattering angle
μ_t = cosine of transmission angle
ξ = size parameter
ϵ = normalized two-norm of relative error
ρ'' = bidirectional reflectivity, sr^{-1}
ρ' = directional-hemispherical reflectivity
σ = scattering coefficient, m^{-1}
φ_d = difference azimuthal angle $\varphi_d = \varphi_{in} - \varphi_r$, rad
φ_{in} = azimuthal angle of incidence, rad
φ_r = azimuthal angle of reflection, rad
Φ = scattering phase function
ψ = pore-space indicator function
ω = scattering albedo
Ω = solid angle, sr

Subscripts

a = absorption
an = analytical
b = blackbody
boundary = medium's boundary
d = diffuse
dep = dependent
e = extinction
EX = experiment
i, j = phase indices (1=void, 2=solid)
in = incoming
int = internal
max = maximum
op = opening
ref = reference
refl = reflection
refr = refraction
s = scattering
sp = specular
tot = total
λ = spectral
∞ = initial

References

[1] Schunk, L., Haeberling, P., Wepf, S., Wuillemin, D., Meier, A., and Steinfeld, A., 2008, "A Receiver-Reactor for the Solar Thermal Dissociation of Zinc Oxide," ASME J. Sol. Energy Eng., **130**, p. 021009.

[2] Wieckert, C., Frommherz, U., Kräupl, S., Guillot, E., Olalde, G., Epstein, M., Santen, S., Osinga, T., and Steinfeld, A., 2007, "A 300 kW Solar Chemical Pilot Plant for the Carbothermic Production of Zinc," ASME J. Sol. Energy Eng., **129**, pp. 190–196.

[3] von Zedtwitz, P., and Steinfeld, A., 2005, "Steam-Gasification of Coal in a Fluidized-Bed/Packed-Bed Reactor Exposed to Concentrated Thermal Radiation-Modeling and Experimental Validation," Ind. Eng. Chem. Res., **44**, pp. 3852–3861.

[4] Piatkowski, N., and Steinfeld, A., 2008, "Solar-Driven Coal Gasification in a Thermally Irradiated Packed-Bed Reactor," Energy Fuels, **22**, pp. 2043–2052.

[5] Osinga, T., Lipiński, W., Guillot, E., Olalde, G., and Steinfeld, A., 2006, "Experimental Determination of the Extinction Coefficient for a Packed-Bed Particulate Medium," Exp. Heat Transfer, **19**, pp. 69–79.

[6] Zhao, C. Y., Lu, T. J., and Hodson, H. P., 2004, "Thermal Radiation in Ultralight Metal Foams With Open Cells," Int. J. Heat Mass Transfer, **47**, pp. 2927–2939.

[7] Kamiuto, K., Iwamoto, M., Nishimura, T., and Sato, M., 1991, "Radiation-Extinction Coefficients of Packed-Sphere Systems," J. Quant. Spectrosc. Radiat. Transf., **45**, pp. 93–96.

[8] Chen, J., and Churchill, S., 1963, "Radiant Heat Transfer in Packed Beds," AIChE J., **9**, pp. 35–41.

[9] Tancrez, M., and Taine, J., 2004, "Direct Identification of Absorption and Scattering Coefficients and Phase Function of a Porous Medium by a Monte Carlo Technique," Int. J. Heat Mass Transfer, **47**, pp. 373–383.

[10] Yang, Y., Howell, J., and Klein, D., 1983, "Radiative Heat Transfer Through a Randomly Packed Bed of Spheres by the Monte Carlo Method," ASME J. Heat Transfer, **105**, pp. 325–332.

[11] Argento, C., and Bouvard, D., 1996, "A Ray Tracing Method for Evaluating the Radiative Heat Transfer in Porous Media," Int. J. Heat Mass Transfer, **39**, pp. 3175–3180.

[12] Chan, C., and Tien, C., 1974, "Radiative Transfer in Packed Spheres," ASME J. Heat Transfer, **96**, pp. 52–58.

[13] Brewster, M., and Tien, C., 1982, "Radiative Transfer in Packed Fluidized Beds—Dependent Versus Independent Scattering," ASME J. Heat Transfer, **104**, pp. 573–579.

[14] Tien, C., 1988, "Thermal Radiation in Packed and Fluidized Beds," ASME J. Heat Transfer, **110**, pp. 1230–1242.

[15] Coquard, R., and Baillis, D., "Radiative Characteristics of Opaque Spherical Particles Beds: A New Method of Prediction," J. Thermophys. Heat Transfer, **18**, pp. 178–186.

[16] Coquard, R., and Baillis, D., 2005, "Radiative Characteristics of Beds of Spheres Containing an Absorbing and Scattering Medium," J. Thermophys. Heat Transfer, **19**, pp. 226–234.

[17] Petrasch, J., Wyss, P., and Steinfeld, A., 2007, "Tomography-Based Monte Carlo Determination of Radiative Properties of Reticulate Porous Ceramics," J. Quant. Spectrosc. Radiat. Transf., **105**, pp. 180–197.

[18] Zeghondy, B., Iacona, E., and Taine, J., 2006, "Determination of the Anisotropic Radiative Properties of a Porous Material by Radiative Distribution Function Identification (RDFI)," Int. J. Heat Mass Transfer, **49**, pp. 2810–2819.

[19] Stanmore, B., 2005, "Review—Calcination and Carbonation of Limestone

During Thermal Cycling for CO_2 Sequestration," Fuel Process. Technol., **86**, pp. 1707–1743.

[20] Farmer, J. T., and Howell, J. R., 1998, "Comparison of Monte Carlo Strategies for Radiative Transfer in Participating Media," Adv. Heat Transfer, **31**, pp. 333–429.

[21] Modest, M., 2003, *Radiative Heat Transfer*, 2nd ed., Academic, San Diego.

[22] Berryman, J., and Blair, S., 1986, "Use of Digital Image Analysis to Estimate Fluid Permeability of Porous Material: Application of Two-Point Correlation Functions," J. Appl. Phys., **60**, pp. 1930–1938.

[23] Petrasch, J., Wyss, P., Stämpfli, R., and Steinfeld, A., 2008, "Tomography-Based Multiscale Analyses of the 3D Geometrical Morphology of Reticulated Porous Ceramics," J. Am. Ceram. Soc., **91**, pp. 2659–2665.

[24] 2003, *Handbook of Fluidization and Fluid-Particle Systems*, W. C. Yang, ed., Marcel Dekker, New York.

[25] Palik, E., 2003, *Handbook of Optical Constants of Solids*, Academic, San Diego.

[26] Querry, M., Osborne, G., Lies, K., Jordon, R., and Coveney, R., 1978, "Complex Refractive Index of Limestone in the Visible and Infrared," Appl. Opt., **17**, pp. 353–356.

[27] Rodriguez-Navarro, C., Rodriguez-Navarro, A., Elert, K., and Sebastian, E., 2004, "Role of Marble Microstructure in Near-Infrared Laser-Induced Damage During Laser Cleaning," J. Appl. Phys., **95**(7), pp. 3350–3357.

[28] Bohren, C., and Huffman, D., 2004, *Absorption and Scattering of Light by Small Particles*, 3rd ed., Wiley, New York.

[29] Tien, C. L., and Drolen, B. L., 1987, "Thermal Radiation in Particulate Media With Dependent and Independent Scattering," Annu. Rev. Numer. Fluid Mech. Heat Transfer, **1**, pp. 1–32.